Research in Astronomy and Astrophysics, 25:025020 (8pp), 2025 February
https://doi.org/10.1088/1674-4527/adb15a
CSTR: 32081.14.RAA.adb15a

Core Mass Function in View of Fractal and Turbulent Filaments and Fibers

Xunchuan Liu (刘训川)[1,2], Tie Liu[1], Xiaofeng Mai[1,3], Yu Cheng[4], Sihan Jiao[5], Wenyu Jiao[1], Hongli Liu[6], and Siju Zhang[7]
[1] Shanghai Astronomical Observatory, Chinese Academy of Sciences, Shanghai 200030, China; liuxunchuan001@gmail.com
[2] Leiden Observatory, Leiden University, P.O. Box 9513, 2300RA Leiden, The Netherlands
[3] Department of Physics, PO Box 64, 00014, University of Helsinki, Finland
[4] National Astronomical Observatory of Japan, 2-21-1 Osawa, Mitaka, Tokyo 181-8588, Japan
[5] National Astronomical Observatories, Chinese Academy of Sciences, Beijing 100012, China
[6] School of Physics and Astronomy, Yunnan University, Kunming 650091, China
[7] Departamento de Astronomía, Universidad de Chile, Las Condes, 7591245 Santiago, Chile
Received 2024 November 27; revised 2025 January 10; accepted 2025 January 29; published 2025 February 21

Abstract

We propose that the core mass function (CMF) can be driven by filament fragmentation. To model a star-forming system of filaments and fibers, we develop a fractal and turbulent tree with a fractal dimension of 2 and a Larson's law exponent (β) of 0.5. The fragmentation driven by convergent flows along the splines of the fractal tree yields a Kroupa-IMF-like CMF that can be divided into three power-law segments with exponents $\alpha = -0.5$, -1.5, and -2, respectively. The turnover masses of the derived CMF are approximately four times those of the Kroupa IMF, corresponding to a star formation efficiency of 0.25. Adopting $\beta = 1/3$, which leads to fractional Brownian motion along the filament, may explain a steeper CMF at the high-mass end, with $\alpha = -3.33$ close to that of the Salpeter IMF. We suggest that the fibers of the tree are basic building blocks of star formation, with similar properties across different clouds, establishing a common density threshold for star formation and leading to a universal CMF.

Key words: stars: formation – stars: kinematics and dynamics – turbulence – stars: luminosity function, mass function – ISM: clouds

1. Introduction

The core mass function (CMF) is a fundamental concept in the study of star formation. Observations indicate that the CMF typically follows a power-law distribution (e.g., Motte et al. 1998; Könyves et al. 2015; Cheng et al. 2018; Pouteau et al. 2022), suggesting a potential link between the CMF and the initial mass function (IMF, Salpeter 1955; Kroupa 2001; Alves et al. 2007; Guszejnov & Hopkins 2015). Exploring the origin of CMF is a key to finding out the fundamental physics that regulate IMF and star formation (Motte et al. 2022). Various theories have been proposed to construct the CMF. Some of the most influential models (e.g., Hennebelle & Chabrier 2008; Hopkins 2012; Haugbølle et al. 2018) begin with the fragmentation of density fluctuations that follow a lognormal distribution, which are produced by three-dimensional (3D) supersonic shocks (e.g., Padoan & Nordlund 2002). These theories focus on general 3D isotropic cases and do not account for the filamentary nature of core-forming clouds or clumps, such as their anisotropy, self-similarity, and low dimensionality.

Filaments are believed to play a very important role in star formation (e.g., Hacar et al. 2023; Pineda et al. 2023, for recent reviews). Filaments are elongated structures (typically longer than 1 pc) that can extend through molecular clouds/clumps. Herschel studies of nearby low-mass star-forming regions (e.g., André et al. 2010; Molinari et al. 2010; Juvela et al. 2012) show that filaments dominate the mass budget of molecular clouds and correspond to the birthplaces of most prestellar cores (e.g., André et al. 2010; Schisano et al. 2014; Könyves et al. 2015). Velocity gradients are common along the filaments. The interferometers make it possible to resolve both nearby and distant filament systems down to core scales (e.g., Beuther et al. 2018; Liu et al. 2020, 2024; Motte et al. 2022; Wells et al. 2024). The distant, massive, dense clumps are also found to consist of hierarchical filamentary hubs and networks (e.g., Peretto et al. 2013; Zhou et al. 2022; Yang et al. 2023). The filament systems can be further divided into fibers in both low- (Hacar et al. 2018) and intermediate- (Yang et al. 2024), as well as high-mass (Liu et al. 2024; Hacar et al. 2024) star-forming regions. Fibers are small branches (typically shorter than 1 pc) of filaments that can only be effectively resolved by interferometers (e.g., Hacar et al. 2024). One of the most important characteristics of fibers is that they may exist in subsonic states (Yue et al. 2021).

Theories of CMF that emphasize the unique role of filaments/fibers are crucial for unveiling the underlying nature of star formation. Myers (2013) explained the CMF through radial accretion onto filaments by introducing an exponential-like stopping time in the accretion process. They presumed that the CMF has a shape similar to that of the IMF. Another

limitation of the model is that Myers (2013) have not considered the fragmentation or the turbulent structure along the filaments, making the model less specific to filamentary structures. Roy et al. (2015) linked the power-law spectrum of density fluctuations along the filament to the CMF. However, they neither explained the origin of the power spectrum in detail, nor how it may be influenced by different turbulence structures. Moreover, they did not consider the fractal nature of filaments. Overall, it is important to establish a theoretical model that can produce an IMF-like CMF while fully accounting for the fractal and turbulent characteristics of filament networks.

In this work, we propose a theoretic model of filament fragmentation that successfully constructs an IMF-like CMF. The paper is organized as follows: in Section 2, we explain why it is theoretically possible to derive the CMF by studying filaments. In Section 3, we develop a model of fractal and turbulent trees to analogize filament/fiber systems, and construct a Kroupa-IMF-like CMF through filament fragmentation. Further, we discuss how to construct a steeper (Salpeter-IMF-like) CMF at the high-mass end based on fractional Brownian motion (fBM, Section 4.1), explain the universality of the CMF (Section 4.2), and present the assumptions and caveats of the model proposed in this work (Section 4.3). In Section 5, we provide a brief summary.

2. Why are Filaments a Stable Texture

The dimension ($n = 0, 1, 2$) of a core, filament, or sheet is defined by the dimensionality of its central part: point, line, or plane. The typical radius (a) and central density (ρ_0) of an isothermal n-dimensional (nD) structure are related by the following equation (Equation (A5))

$$a \propto \rho_0^{-1/2}, \tag{1}$$

where the power-law index is independent of the dimension. The mass (or line mass/surface density) enclosed within a radius of a for the nD structures ($n = 0, 1, 2$), denoted as η_{nd}, can be estimated as

$$\eta_{nd} \sim \rho_0 a^{3-n} \propto \rho_0^{(n-1)/2}. \tag{2}$$

For $n = 2$, it is evident that η_{2d} is an increasing function of ρ_c. This implies that reducing the scale a (and thus increasing ρ_0) of a sheet will require a higher surface density to make it gravitationally bound. Therefore, a two-dimensional (2D) sheet is difficult to compress continuously under its own self-gravity. For $n = 0$, the solution to Equation (A2) is the well-known Bonnor–Ebert (B-E) sphere (Bonnor 1956), for which $\eta_{0d} \propto \rho_0^{-1/2}$. When a sphere in equilibrium is slightly compressed due to perturbations, the critical mass becomes smaller than the real mass, triggering an accelerating collapse.

For $n = 1$, which corresponds to the case of an isolated filament, η_{1d} is independent of the filament width (Equation (2)). In equilibrium, the radial density profile is described by the Plummer function (Plummer 1911), as confirmed by observations (e.g., Nutter et al. 2008; Arzoumanian et al. 2011; Liu et al. 2021; André et al. 2022). The precise value of the critical line mass of a filament is given by (Ostriker 1964; Inutsuka & Miyama 1997; André et al. 2014)

$$\eta_{1d}^{\rm crit} = \frac{2\delta^2}{G}. \tag{3}$$

Here, in the case of thermal support, δ represents the sound speed (c_s); for turbulent support, the turbulent velocity dispersion ($\delta_{\rm turb}$) should be taken into account: $\delta^2 = c_s^2 + \delta_{\rm turb}^2$. As an example calculation of $\eta_{1d}^{\rm crit}$, for $\delta = 0.3\ {\rm km\ s^{-1}}$, $\eta_{1d}^{\rm crit} \sim 40\ M_\odot\ {\rm pc^{-1}}$.

Overall, 2D sheets are difficult to be compressed by self-gravity. One-dimensional (1D) filaments and zero-dimensional cores are two key types of self-gravitating structures. The instability of cores finally leads to formation of stars. However, a filament cannot undergo a sustained global collapse. Observations show that filaments can be disrupted by strong impacts, such as the expansion of H II regions (e.g., Zhang et al. 2016; Zhou et al. 2022). However, even under such strong impact, the clumps/cores in the compressed gas may still originate from the sweeping up of pre-existing fragments (e.g., Zhang et al. 2024). These analyses, supported by observational evidence, suggest that filaments are stable structures, resistant to disruption by both internal gravity and external pressures (e.g., turbulence and stellar feedback). As a result, they help preserve the initial seeds of star formation.

3. CMF of Filaments

3.1. Fragmentation Along a Filament of Infinite Length

Larson's law (Larson 1981) yields that

$$\sigma \propto L^{\beta} \tag{4}$$

where σ is the velocity dispersion and L is the size of the cloud. The original value of β given by Larson (1981) is 0.38, which is close to the value (1/3) expected for standard Kolmogorov turbulence (Kolmogorov 1941; Frisch 1995). For compressible fluid (Burgers turbulence), $\beta = 0.5$ (Burgers 1948). We adopt $\beta = 0.5$ for the turbulent and gravity-bound star-forming clouds (e.g., Heyer et al. 2009).

An isolated filament can be treated as a 1D structure, with the velocity along the filament following the turbulent motion described by Larson's law (Equation (4)). The velocity distribution along the filament can then be modeled as 1D random walk in Brownian motion,

$$\langle v^2 \rangle \propto L. \tag{5}$$

The probability distribution of the zero-crossing intervals $L_{\rm Z}$ follows (Wiener 1923; Gardiner 2009)

$$P(L_{\rm Z}) \propto L_{\rm Z}^{-1.5}, \tag{6}$$

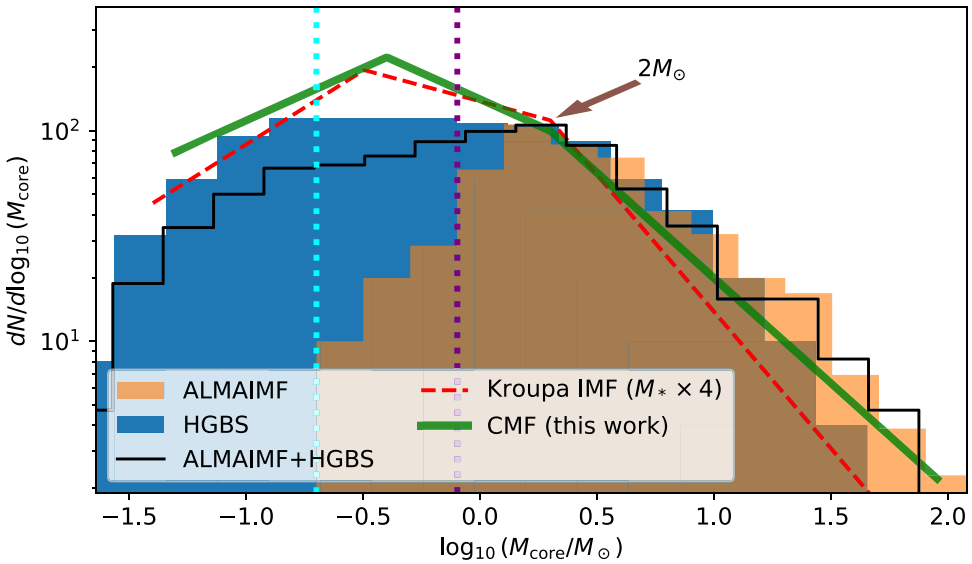

Figure 1. The CMF of the ALMA-IMF survey (Motte et al. 2022; Louvet et al. 2024) is shown in orange, and that of the Herschel HGBS survey (André et al. 2010; Könyves et al. 2015) in blue. We adopt the full core catalog of the ALMA-IMF survey for all 15 massive star formation regions, and the core catalog for the Aquila cloud complex covered by HGBS. The cyan and purple dotted vertical lines indicate the 90% completeness core mass for the HGBS and ALMA-IMF surveys, respectively. The CMFs of both data sets exhibit a similar turnover mass at $\sim 2M_\odot$, consistent with the value predicted in this work (Section 3.3). The CMFs of the two data sets also coincidentally have a similar number of cores around the turnover mass. Therefore, we combine them directly with equal weightings. The black line represents the CMF of the combined data set (with the y-axis values adjusted so that it reaches 100 at 2 $M_\odot$). The red dashed line represents the shifted Kroupa IMF, with the stellar mass multiplied by a factor of four. The values of α for the shifted Kroupa IMF within the three intervals (from left to right) are -0.3, -1.3, and -2.3, respectively (Kroupa 2001). The green line represents the theoretical CMF of this work (Equation (33)).

and the average number of the zero-crossing events ($\langle N_Z \rangle$) within an interval of length L is given by

$$\langle N_Z(L) \rangle \propto L^{0.5}. \tag{7}$$

We assume that a filament is radially supported by thermal dispersion with a nearly constant $\eta_{1d}^{\rm crit}$. The fragmentation of the filament is driven by convergent flow along the filament around the zero-crossing points of the tangential velocity. The mass of the fragmentation should be proportional to L_Z. The mass function of the fragmentation along a filament of infinite length (FMF) is (Equation (6))

$$\mathrm{FMF}(M) \propto M^{-1.5}. \tag{8}$$

The FMF is noticeably flatter than the observed CMF and IMF at the high-mass end (e.g., André et al. 2019, see also Figure 1). Moreover, the integral of the above equation diverges. In realistic scenarios, there should be cutoffs at both the high-mass and low-mass ends, denoted as $M_{\rm min}$ and $M_{\rm max}$, respectively. We adopt:

$$M_{\rm min} \sim \eta_{1d}^{\rm crit} \mathcal{W}, \tag{9}$$

$$M_{\rm max} \propto \eta_{1d}^{\rm crit} L, \tag{10}$$

where $\mathcal{W}$ is the width of the filament.

3.2. CMF of a Fractal Tree of Filaments

3.2.1. A Tree Embedded in a Star-forming Cloud/Clump

For a massive clump supported by turbulence as described by Equation (4), the virial equilibrium requires

$$\frac{GM_C}{r_C} \propto r_C, \tag{11}$$

where M_C and r_C represent the mass and radius of the clump, respectively. It yields

$$r_C \propto M_C^{1/2}. \tag{12}$$

The density profile of the clump (ρ_C) is

$$\rho_C \sim M_C / r_C^3 \propto r_C^{-1}. \tag{13}$$

We assume that a star-forming cloud/clump is dominated by filamentary structures composed of fibers that are thermally supported, with similar critical line masses. It implies that the filament/fiber system should have a fractal dimension ($D_{\rm fil}$) given by

$$D_{\rm fil} = \frac{\log(M_C)}{\log(r)} = 2. \tag{14}$$

3.2.2. Construct the Fractal Tree

The fractal structure of the filament/fiber system plays a critical role in regulating the statistical properties of core

masses, and thus the FMF in Equation (8) cannot be directly used to construct the CMF. Here, we explore the CMF through constructing a model of a self-similar tree. The basic blocks of a tree are fibers with constant length ($\mathcal{L}$) and line mass. These fibers merge progressively to form increasingly larger branches (sub-trees), ultimately shaping the tree. The widths of the fibers ($\mathcal{W}$) may decrease as they evolve. The fibers along which cores/stars begin to appear are denoted as $\mathcal{T}_1$ and its length is denoted as $\mathcal{L}_1$. Thus, the entire tree represents a core/star-forming structure in a dynamically evolving process. Each sub-tree has a longest path, denoted as the spline of the sub-tree. A sub-tree is denoted as $\mathcal{T}_i$ if its spline has a length of $\mathcal{L}_i = i \times \mathcal{L}_1$. Here, i is a natural number ($i = 1, 2, 3, \ldots$). The whole tree, with a spline length of $\mathcal{L}_\mathcal{N} = \mathcal{N} \times \mathcal{L}_1$, is denoted as $\mathcal{T}_\mathcal{N}$. We require

$$\mathcal{L}_\mathcal{N} \sim R_C, \tag{15}$$

where R_C is the cloud/clump size. Equations (10) and (15), as well a constant η_{1d}, imply that the maximum core mass of the clump ($M^C_{\rm max}$) follows

$$M^C_{\rm max} \propto M_C^{1/2}. \tag{16}$$

This is consistent with the results of simulations (e.g., Bonnell et al. 2004) and observations (e.g., Anderson et al. 2021; Morii et al. 2023; Yan et al. 2023). A recent statistical result based on data from the Herschel HGBS survey (André et al. 2010) and the ALMA-IMF survey (Motte et al. 2022) also yields a power-law index ∼0.5 (Jiao et al., submitted; private communication).

To construct the tree, we proceed from $\mathcal{T}_1$ at the tail of the spline of $\mathcal{T}_\mathcal{N}$. At the $i_{\rm th}$ step, the head of $\mathcal{T}_i$ would intersect with the heads of smaller sub-trees ($\mathcal{T}_j$ with $j < i \leqslant \mathcal{N}$). Each $\mathcal{T}_j$ appears with a probability given by

$$p_j = \frac{bj^{-\gamma}}{\zeta(\gamma)}. \tag{17}$$

Here, $\zeta(\gamma) = \sum_j j^{-\gamma}$, and b can be interpreted as the average number of sub-trees that join at each step. Denote $\mathcal{M}_i$ as the mass of $\mathcal{T}_i$. We have

$$\mathcal{M}_{i+1} \sim \mathcal{M}_i + 1 + \sum_1^i p_j \mathcal{M}_j. \tag{18}$$

$\mathcal{M}_i$ should be proportional to $\mathcal{L}_i^{D_{\rm fil}}$ (Equation (14)), that is

$$\mathcal{M}_i \propto \mathcal{L}_i^2, \tag{19}$$

which is consistent with the statistical results of the observations (Hacar et al. 2023). It leads to

$$(i+1)^{D_{\rm fil}} \propto i^{D_{\rm fil}} + i^{D_{\rm fil}+1-\gamma} b/\zeta(\gamma)/(D_{\rm fil}+1-\gamma), \tag{20}$$

where $1 < D_{\rm fil} \leqslant 2$. It requires that $\gamma = 2$, and $D_{\rm fil} = b/\zeta(2)/(D_{\rm fil}-1)$, which leads to

$$D_{\rm fil} = \sqrt{b/\zeta(2) + 0.25} + 0.5. \tag{21}$$

Adopting $b = 2\zeta(2)$ yields a $D_{\rm fil}$ of 2.

3.2.3. CMF at the High-mass End

On average, the entire tree $\mathcal{T}_\mathcal{N}$ can be divided into N_i sub-trees $\mathcal{T}_i$, where N_i is estimated from Equation (19) as

$$N_i \sim \left(\frac{\mathcal{N}}{i}\right)^{D_{\rm fil}} \propto \mathcal{L}_i^{-D_{\rm fil}}. \tag{22}$$

It directly yields a spline length function (SLF) of

$$\mathrm{SLF}(\mathcal{L}) \propto \mathcal{L}^{-2}. \tag{23}$$

The high-mass cutoff for the CMF along the spline and across the entire branches of $\mathcal{T}_i$, derived from Equation (10), is

$$M^i_{\rm max} \propto \mathcal{L}_i \propto i. \tag{24}$$

Equations (7), (8), (23), and (24) lead to a high-mass-end CMF (denoted as $\mathrm{CMF^H}$)

$$\begin{aligned}\mathrm{CMF^H}(M) &\propto \int_M x^{-2} x^{0.5} \mathrm{FMF}(x)\,dx \\ &\propto M^{-2}.\end{aligned} \tag{25}$$

It means that the power-law index of the CMF at the high-mass end is determined by that of the SLF. The massive cores are likely to be situated at the convergent hubs, where different branches intersect.

3.2.4. CMF at the Low-mass End

We assume that the density along the spline of a $\mathcal{T}_i$ (denoted as ρ_i) follows

$$\rho_i \propto i^p, \tag{26}$$

and $\rho_\mathcal{N}$ and ρ_1 are proportional to the densities at the central and boundary of the cloud/clump, respectively. From Equation (13), we have

$$\rho_\mathcal{N}/\rho_1 \propto \mathcal{N}, \tag{27}$$

which further requires that

$$\rho_i \propto i. \tag{28}$$

From Equation (1), the width of the spline of $\mathcal{T}_i$ (denoted as $\mathcal{W}_i$) can be expressed as

$$\mathcal{W}_i \propto i^{-0.5}. \tag{29}$$

It sets a low-mass cutoff for the CMF along the spline and across the entire branches of $\mathcal{T}_i$ as

$$M^i_{\rm min} \propto \mathcal{W}_i \propto i^{-0.5}. \tag{30}$$

Note that $M^i_{\rm min}$ can be interpreted as the thermal Jeans mass corresponding to ρ_i. Low-mass cores with masses $\sim M^i_{\rm min}$ are primarily produced along the spline of $\mathcal{T}_i$. The CMF at the low-mass end ($\mathrm{CMF^L}$) can then be derived from Equations (7), (14), (22), (29), and (30) as

$$\mathrm{CMF^L}(M) \propto N_i \left(\frac{i}{\mathcal{W}_i}\right)^{0.5} \left(\frac{dM^i_{\rm min}}{di}\right)^{-1} \propto M^{-0.5}. \tag{31}$$

The longest (and thus most evolved) spline of the tree contributes to the formation of cores with both the lowest and highest masses. The power-law index of the derived $\mathrm{CMF^L}$ is compatible with that of the Kroupa IMF at the low-mass end (-0.3 to -1.3).

3.3. The Merged CMF and its Turnover Masses

It is not straightforward to merge $\mathrm{CMF^L}$ and $\mathrm{CMF^H}$, as most of the quantities discussed are in very general cases without characteristic scales. This is somewhat reasonable, as both filaments and fragmentation are universal phenomena that span a wide range of scales. For filament/fiber systems within star-forming clouds/clumps that we focus on here, there exist some characteristic scales. The fractal tree constructed above has two important characteristic scales: the typical width and length of $\mathcal{T}_1$, which determine the $M^1_{\rm min}$ and $M^1_{\rm max}$, respectively. The CMF is expected to be divided into three segments by $M^1_{\rm min}$ and $M^1_{\rm max}$, with each segment having a different power-law index (α). The power-law indices at the low-, intermediate-, and high-mass ends are adopted as -0.5 (Equation (31)), -1.5 (Equation (8)), and -2 (Equation (25)), respectively.

The filament length and width of $\mathcal{T}_i$ are uncertain. We assume that the "typical width (0.1 pc)" of the Herschel filaments (André et al. 2022) is contributed to the elemental fibers ($\mathcal{T}_1$) that intersect with the splines of the filaments, with a length-to-width aspect ratio of five. Then, $\mathcal{L}_1$ and $\mathcal{W}_1$ are estimated to be 10,000 au ($\sim$0.05 pc) and 2000 au, respectively. This is consistent with the observational results from SMA and ALMA for nearby clouds and distant massive clumps (e.g., Yue et al. 2021; Yang et al. 2024). A typical temperature of 25 K of molecular gas corresponds to a critical line mass $\eta^{\rm crit}_{1d} = 40 M_\odot\,{\rm pc}^{-1}$ (e.g., Yang et al. 2024). We thus further estimate

$$\begin{cases} M^1_{\rm max} \sim \eta^{\rm crit}_{1d}\,\mathcal{L}_1 \sim 2\,M_\odot, \\ M^1_{\rm min} \sim \eta^{\rm crit}_{1d}\,\mathcal{W}_1 \sim 0.4\,M_\odot. \end{cases} \tag{32}$$

Then we have

$$\mathrm{CMF}(M) = \begin{cases} M^{-0.5} & \text{for } M < 0.4\,M_\odot \\ M^{-1.5} & \text{for } 0.4 < M < 2\,M_\odot \\ M^{-2} & \text{for } M > 2\,M_\odot \end{cases}. \tag{33}$$

The turnover mass $M^1_{\rm max} \sim 2\,M_\odot$ is consistent with the CMFs given by the observations of the Herschel HGBS survey (Motte et al. 2022; Louvet et al. 2024) and the ALMA-IMF survey (André et al. 2010; Könyves et al. 2015) (Figure 1). The CMF in Equation (33) is also similar to that of the Kroupa IMF (Kroupa 2001), except for a multiplication of the star mass of the Kroupa IMF by a factor of four, which corresponds to a core-to-star mass efficiency of 25% (Figure 1).

The small discrepancy between the derived CMF (Equation (33)) and the shifted Kroupa IMF may contribute to the nonlinear relationship between the CMF and the IMF (e.g., Holman et al. 2013; Guszejnov & Hopkins 2015). The overpopulation of the derived CMF, compared to the observations (Figure 1), may contribute to the miscounting of the flattened cores of $\mathcal{T}_1$, due to the limited angular resolution of single-dish telescopes and the missing flux effect of interferometers (e.g., Sahu et al. 2023).

4. Discussion

4.1. Fragmentation Under Fractional Brownian Motion

Above, $\mathrm{CMF^H}$ is obtained by convolving the FMF and SLF, with the result depending solely on the SLF (Section 3.2.3). It matches observations of massive star-forming regions, but is slightly flatter than that of nearby low-mass star-forming regions (Figure 1). Here, we note that a steeper $\mathrm{CMF^H}$ can be reproduced by the turbulence fragmentation of isolated filaments.

In Section 3.1, we considered only $\beta = 0.5$. For other values of β (e.g., $\beta = 0.33$ for Kolmogorov turbulence), we modeled the velocity distribution along the filament as fBM,

$$\langle v^2 \rangle \propto L^{2\mathcal{H}}, \tag{34}$$

where $\mathcal{H} = \beta$ is the Hurst exponent. Similar to Equations (6) and (7), for fBM (Mandelbrot & Van Ness 1968; Rambaldi & Pinazza 1994; Biagini et al. 2008), the probability distribution of the zero-crossing intervals ($P_{\mathcal{H}}(L_{\rm Z})$) and the average number of zero-crossing events ($\langle N_{{\rm Z};\mathcal{H}}(L)\rangle$) satisfy:

$$P_{\mathcal{H}}(L_{\rm Z}) \propto L_{\rm Z}^{-(2-\mathcal{H})}, \tag{35}$$

$$\langle N_{{\rm Z};\mathcal{H}}(L)\rangle \propto L^{1-\mathcal{H}}, \tag{36}$$

respectively. The first-level fragmentation by converging flows along an isolated filament (Equation (35)) leads to a power-law index of FMF of $-(2-\mathcal{H})$. The local velocity gradient could be steeper than the global velocity gradient around the zero-crossing points, leading to second-level fragmentation. We assume that second-level fragmentation tends to break a segment of length L into one larger sub-segment, with a length distribution following Equation (35), along with several smaller sub-segments. At the long-segment end, the length of the sub-segment (l) follows a probability distribution given by

$$\mathrm{FMF}_2(l) \propto \frac{P_{\mathcal{H}}(l)}{\langle N_{{\rm Z};\mathcal{H}}(l)\rangle} \propto l^{-(3-2\mathcal{H})}, \tag{37}$$

which results in a $\mathrm{CMF^H}$ with an exponent $\alpha = -(3-2\mathcal{H})$. For Kolmogorov turbulence ($\mathcal{H} = \beta = 1/3$), $\alpha = -2.33$, very close to the power-law index of the Salpeter IMF (-2.35) (Salpeter 1955) and the Kroupa IMF (-2.3) at the high-mass end. For Burgers turbulence ($\mathcal{H} = \beta = 1/2$), it again gives a top-heavy CMF with $\alpha = -2$. These results suggest that the CMF at the high-mass end may be linked to some fundamental and universal mechanisms of star formation. We propose an α

between -2 and $-(3–2\beta)$, depending on how the structures of the turbulence and the filament system are formed.

4.2. Why the Fractal Tree is Universal

The column density of the splines of $\mathcal{T}_i$ (denoted as Σ_i) is (Equations (28) and (29))

$$\Sigma_i \propto \rho_i \mathcal{W}_i \propto i^{0.5}. \tag{38}$$

The distribution of Σ_i can be expressed as

$$dN(\Sigma_i) \propto N_i \mathcal{L}_i \mathcal{W}_i di \propto \Sigma_i^{-1} d\log(\Sigma_i), \tag{39}$$

yielding a column density probability distribution function (N-PDF) power-law index (ω) of -1. Observations show that the value of ω, at the high-column-density end influenced by star formation (e.g., Scalo et al. 1998; Kainulainen et al. 2009), exhibits a decreasing trend (from -1 to -3) over the evolution of the cloud/clump, reaching a value of -1 in the early stages (e.g., Stutz & Kainulainen 2015). It confirms that the fractal tree we have established captures the key properties of the early-stage structures that harbor the seeds of star formation.

The universality of the turnover masses of the CMF derived in Section 3 relies on that of $\mathcal{T}_1$ (Equation (32)). The host cloud/clump of $\mathcal{T}_i$ has an average volume density (n_i) of

$$n_{\rm Ci} \sim M_i/\mathcal{L}_i^3 \sim n_{\rm C1}/i, \tag{40}$$

with

$$n_{\rm C1} \sim \eta_{1d}^{\rm crit}/\mathcal{L}_1^2 \sim 10^5 \quad {\rm cm}^{-3}. \tag{41}$$

The mass of a star-forming tree ($\mathcal{M}_{\mathcal{N}}$) is dominated by the mass of all the $\mathcal{T}_1$ branches of the tree. The star formation rate (SFR) follows

$${\rm SFR} \propto \mathcal{M}_{\mathcal{N}} \propto M_{n>n_{\rm C1}}, \tag{42}$$

where

$$M_{n>n_{\rm C1}} = \int_{n>n_{\rm C1}} \rho dV. \tag{43}$$

We assume that $n_{\rm C1}$ is the density threshold above which star-forming trees can be established, starting from $\mathcal{T}_1$. If these trees share similar density thresholds and evolutionary processes, a universal density threshold for star formation may be expected. This is consistent with the concept of the well-known star formation law, which describes the linear correlation between dense gas surface density and SFR (Kennicutt 1998; Gao & Solomon 2004). Commonly used dense gas tracers, such as HCO^+ (1–0) and HCN (1–0) (e.g., Gao & Solomon 2004; Shimajiri et al. 2017; Rybak et al. 2022), have critical densities (approximately 10^5 cm^{-3}; Mangum & Shirley 2015) similar to the value of $n_{\rm C1}$. We thus propose that the universality of the CMF is linked to that of the star formation law.

4.3. Assumptions and Caveats

Here, we list the key assumptions made in establishing the model of this work. (1) The density and turbulent structures of a cloud/clump are dominated by those of a hierarchically structured filamentary tree. (2) The tree can be resolved into fibers that are radially supported by thermal motion. (3) Although the critical line masses of fibers and splines are maintained throughout the evolution of the tree, their density gradually increases. (4) Jeans fragmentation of the evolved splines and convergent flows along them contribute to the formation of low-mass and high-mass cores, respectively.

The first assumption posits that the 1D fibers merge into 2D fractal filamentary trees that fully extend within the clouds/clumps. Since a 2D sheet is difficult to compress under self-gravity (Section 2), the filamentary trees play the roles of both 2D and 1D structures during the process of gas collection from 3D clouds/clumps into point-like protostars. The second assumption is pretty strong. Fibers in low-mass clouds have been observationally shown to be subsonic (Yue et al. 2021), which is a key characteristic of fibers. Filaments in intermediate-mass star-forming regions can also be resolved into fibers that are narrow in line width (Yang et al. 2024). Some observational evidence suggests that filaments in star-forming regions with high-mass young protostars could also be resolved into subsonic fibers by ALMA (Hacar et al. 2024). However, to date, no systematic observational studies of remote high-mass star formation regions have been conducted on this issue, and we remain to treat it as an assumption. The third assumption depends not only on the spatial distribution of the fibers, but also on how they dynamically merge into a filamentary tree. The detailed processes remain poorly understood, both observationally and theoretically. The fourth assumption is essentially the key concept of this model. One of the inferences of the fourth assumption is that a young massive protostar should be accompanied by some low-mass protostars of similar evolutionary age around its birthplace. This is supported by the recent detection of both a low-mass hot corino and a high-mass hot core within the same protocluster (Liu et al. 2023).

There are several caveats associated with the model presented in this work. Notably, the potentially important role of magnetic fields has not been considered. Molecular clouds with strong magnetic fields may require a higher threshold density for the formation of star-forming filamentary structures, thereby further altering the CMF. For simplicity, we have also not considered the effects of feedback from high-mass protostars. Although filaments can be resistant to disruption by both internal gravity and external pressures (Section 2), the strong influence of expanding H II regions may alter the topology and CMF of the filaments. Additionally, the thermal feedback from protoclusters may lead to higher core masses by increasing the critical line masses of filaments and fibers. At present, this model remains in the realm of theoretical

exploration and requires further observations to help validate its assumptions and inferences.

5. Summary

In this work, we propose that the filament system is a stable structure that preserves the initial seeds of star formation. We model a fractal and turbulent tree of filaments/fibers with a fractal dimension of 2 and a Larson's law exponent (β) of 0.5 to explore the CMF under turbulent fragmentation along the filaments. A Kroupa-IMF-like CMF can be produced. The CMF at the low-mass end ($<0.4\,M_{\odot}$) is influenced by the turbulent fragmentation of sub-trees at different evolutionary stages, and thus by variations in filament widths. The CMF at the high-mass end ($>2\,M_{\odot}$) depends on the fractal dimension of the tree. By adopting a β of $1/3$, it is possible to construct a Salpeter-IMF-like CMF at the high-mass end. The turnover masses of the CMF depend on the properties of the fibers on which cores/stars begin to form. We suggest that these fibers ($\mathcal{T}_1$) are the basic building blocks of star formation, sharing similar properties across different clouds, motivated by the universality of the so-called star formation law. These fibers set a common threshold for star formation, leading to a universal CMF.

Acknowledgments

X.L. acknowledges the support of the Strategic Priority Research Program of the Chinese Academy of Sciences under grant No. XDB0800303, the National Key R&D Program of China under grant No. 2022YFA1603100, and the National Natural Science Foundation of China (NSFC, Grant No. 12203086). We also thank the anonymous referee for the insightful comments, which helped refine this work.

Appendix
Structure Density Profile

Denote r the radius (or width/thickness), and ρ the density of the nD structures. For isothermal cases, the dynamic equilibrium between gravity and the pressure gradient requires that

$$r^{-(2-n)}\int_0^r l^{2-n}\rho\, dl = -A\frac{d\rho}{\rho\, dr}, \tag{A1}$$

where $A = c_n\frac{kT}{\mu m_{\rm H}G}$, k is the Boltzmann constant, G is the gravitational constant, μ is the mean molecular weight, $m_{\rm H}$ is the mass of a hydrogen atom, and T is the temperature. Here, c_n is 1, 2, and 2π for $n = 0$, 1, 2, respectively. Denote $\rho = e^y$. By differentiating both sides, the above equation (Equation (A1)) becomes

$$\frac{d^2y}{dr^2} + (2-n)\frac{dy}{rdr} = -\frac{e^y}{A}. \tag{A2}$$

For small r close to the center of the structure, through expanding y as

$$y = y_0 - \frac{1}{a^2}r^2 + O(r^2), \tag{A3}$$

and substituting it into Equation (A2), we obtain

$$(6-2n)/a^2 \sim e^{y_0}/A = \rho_0/A. \tag{A4}$$

Here, ρ_0 represents the density at $r = 0$. The typical scale of the structures can be estimated to be a (half width at $1/e$ of the maximum). From Equation (A4), we have

$$a \propto A^{1/2}\rho_0^{-1/2}. \tag{A5}$$

For a 2D sheet ($n = 2$), the analytical solution to Equation (A2) can be expressed as

$$y(r) = \rho_0\left(1 - \tanh^2\left(\frac{1}{2}\sqrt{\frac{2\rho_0}{A}}\, r\right)\right). \tag{A6}$$

From Equation (2), we have $\eta_{2d} \propto \rho_0^{1/2}$, which can be directly examined using Equation (A6).

References

Alves, J., Lombardi, M., & Lada, C. J. 2007, A&A, 462, L17
Anderson, M., Peretto, N., Ragan, S. E., et al. 2021, MNRAS, 508, 2964
André, P., Arzoumanian, D., Könyves, V., Shimajiri, Y., & Palmeirim, P. 2019, A&A, 629, L4
André, P., Di Francesco, J., & Ward-Thompson, D. 2014, in Protostars and Planets VI, ed. H. Beuther et al. (Tucson, AZ: Univ. Arizona Press), 27
André, P., Men'shchikov, A., Bontemps, S., et al. 2010, A&A, 518, L102
André, P. J., Palmeirim, P., & Arzoumanian, D. 2022, A&A, 667, L1
Arzoumanian, D., André, P., Didelon, P., et al. 2011, A&A, 529, L6
Beuther, H., Mottram, J. C., Ahmadi, A., et al. 2018, A&A, 617, A100
Biagini, F., Hu, Y., ksendal, B., & Zhang, T. 2008, Stochastic Calculus for Fractional Brownian Motion and Applications (Berlin: Springer)
Bonnell, I. A., Vine, S. G., & Bate, M. R. 2004, MNRAS, 349, 735
Bonnor, W. B. 1956, MNRAS, 116, 351
Burgers, J. M. 1948, in in Advances in Applied Mechanics, ed. R. V. Mises & T. V. Krmn, Vol. 1 (Amsterdam: Elsevier), 171
Cheng, Y., Tan, J. C., Liu, M., et al. 2018, ApJ, 853, 160
Frisch, U. 1995, Turbulence: The Legacy of A. N. Kolmogorov (Cambridge: Cambridge Univ. Press)
Gao, Y., & Solomon, P. M. 2004, ApJ, 606, 271
Gardiner, C. W. 2009, Stochastic Methods: A Handbook for the Natural and Social Sciences (4th ed.; Berlin: Springer)
Guszejnov, D., & Hopkins, P. F. 2015, MNRAS, 450, 4137
Hacar, A., Clark, S. E., Heitsch, F., et al. 2023, in ASP Conf. Ser. 534, Protostars and Planets VII, ed. S. Inutsuka et al. (San Francisco, CA: ASP), 153
Hacar, A., Socci, A., Bonanomi, F., et al. 2024, A&A, 687, A140
Hacar, A., Tafalla, M., Forbrich, J., et al. 2018, A&A, 610, A77
Haugbølle, T., Padoan, P., & Nordlund, Å. 2018, ApJ, 854, 35
Hennebelle, P., & Chabrier, G. 2008, ApJ, 684, 395
Heyer, M., Krawczyk, C., Duval, J., & Jackson, J. M. 2009, ApJ, 699, 1092
Holman, K., Walch, S. K., Goodwin, S. P., & Whitworth, A. P. 2013, MNRAS, 432, 3534
Hopkins, P. F. 2012, MNRAS, 423, 2037
Inutsuka, S.-i., & Miyama, S. M. 1997, ApJ, 480, 681
Juvela, M., Ristorcelli, I., Pagani, L., et al. 2012, A&A, 541, A12
Kainulainen, J., Beuther, H., Henning, T., & Plume, R. 2009, A&A, 508, L35
Kennicutt, R. C. J. 1998, ApJ, 498, 541
Kolmogorov, A. 1941, DoSSR, 30, 301
Könyves, V., André, P., Men'shchikov, A., et al. 2015, A&A, 584, A91
Kroupa, P. 2001, MNRAS, 322, 231

Larson, R. B. 1981, MNRAS, 194, 809
Liu, M., Qin, S.-L., Liu, T., et al. 2023, ApJ, 958, 174
Liu, T., Evans, N. J., Kim, K.-T., et al. 2020, MNRAS, 496, 2790
Liu, X., Liu, T., Zhu, L., et al. 2024, RAA, 24, 025009
Liu, X. C., Wu, Y., Zhang, C., et al. 2021, ApJ, 912, 148
Louvet, F., Sanhueza, P., Stutz, A., et al. 2024, A&A, 690, A33
Mandelbrot, B. B., & Van Ness, J. W. 1968, SIAMR, 10, 422
Mangum, J. G., & Shirley, Y. L. 2015, PASP, 127, 266
Molinari, S., Swinyard, B., Bally, J., et al. 2010, PASP, 122, 314
Morii, K., Sanhueza, P., Nakamura, F., et al. 2023, ApJ, 950, 148
Motte, F., Andre, P., & Neri, R. 1998, A&A, 336, 150
Motte, F., Bontemps, S., Csengeri, T., et al. 2022, A&A, 662, A8
Myers, P. C. 2013, ApJ, 764, 140
Nutter, D., Kirk, J. M., Stamatellos, D., & Ward-Thompson, D. 2008, MNRAS, 384, 755
Ostriker, J. 1964, ApJ, 140, 1056
Padoan, P., & Nordlund, Å. 2002, ApJ, 576, 870
Peretto, N., Fuller, G. A., Duarte-Cabral, A., et al. 2013, A&A, 555, A112
Pineda, J. E., Arzoumanian, D., Andre, P., et al. 2023, in ASP Conf. Ser. 534, Protostars and Planets VII, ed. S. Inutsuka et al. (San Francisco, CA: ASP), 233
Plummer, H. C. 1911, MNRAS, 71, 460
Pouteau, Y., Motte, F., Nony, T., et al. 2022, A&A, 664, A26
Rambaldi, S., & Pinazza, O. 1994, PhyA, 208, 21
Roy, A., André, P., Arzoumanian, D., et al. 2015, A&A, 584, A111
Rybak, M., Hodge, J. A., Greve, T. R., et al. 2022, A&A, 667, A70
Sahu, D., Liu, S.-Y., Johnstone, D., et al. 2023, ApJ, 945, 156
Salpeter, E. E. 1955, ApJ, 121, 161
Scalo, J., Vázquez-Semadeni, E., Chappell, D., & Passot, T. 1998, ApJ, 504, 835
Schisano, E., Rygl, K. L. J., Molinari, S., et al. 2014, ApJ, 791, 27
Shimajiri, Y., André, P., Braine, J., et al. 2017, A&A, 604, A74
Stutz, A. M., & Kainulainen, J. 2015, A&A, 577, L6
Wells, M. R. A., Beuther, H., Molinari, S., et al. 2024, A&A, 690, A185
Wiener, N. 1923, JMaPh, 2, 131
Yan, Z., Jerabkova, T., & Kroupa, P. 2023, A&A, 670, A151
Yang, D., Liu, H.-L., Liu, T., et al. 2024, ApJ, 976, 241
Yang, D., Liu, H.-L., Tej, A., et al. 2023, ApJ, 953, 40
Yue, N.-N., Li, D., Zhang, Q.-Z., et al. 2021, RAA, 21, 024
Zhang, C.-P., Li, G.-X., Wyrowski, F., et al. 2016, A&A, 585, A117
Zhang, S., Liu, T., Wang, K., et al. 2024, MNRAS, 535, 1364
Zhou, J.-W., Liu, T., Evans, N. J., et al. 2022, MNRAS, 514, 6038